Analysis of Heat and Mass Transfer for a Single-Planar-Anode-Supported Solid Oxide Fuel Cell Considering Internal Reforming

ZHANG Zhuqian[1,2,*], WANG Yulei[1,2], BA Liming[3]

1. Institute of Thermal Engineering, School of Mechanical Electronic and Control Engineering, Beijing Jiaotong University, Beijing 100044, China
2. Beijing Key Laboratory of Flow and Heat Transfer of Phase Changing in Micro and Small Scale, Beijing 100044, China
3. National Institute of Clean- and-Low-Carbon Energy, Beijing 102211, China

Abstract: The temperature uniformity and component concentration distributions in solid oxide fuel cells during operating processes can influence the cell electrochemical and thermal characteristics. A three-dimensional thermal-fluid numerical model including electrochemical reactions and water-gas-shift (WGS) reaction for a single channel solid oxide fuel cell was developed to study the steady-state characteristics, which include distributions of the temperature (T), temperature gradient ($\Delta T/\Delta x$), and fuel utilization. It was shown that the maximum temperature (T_{max}) changed with operating voltage and the maximum temperature gradient ($(\Delta T/\Delta x)_{max}$) occurred at the inlet of the channel of a solid oxide fuel cell by simulation. Moreover, the natural convection condition had a great influence on T and $\Delta T/\Delta x$. The thermal stress generated by temperature differences was the key parameter and increasing the convection heat-transfer coefficient can greatly reduce the thermal stress. In addition, the results also showed that there were lower temperature gradients and lower current density at high working voltage; therefore, choosing the proper operating voltage can obtain better cell performance.

1. Introduction

Conventional power-generation methods rely on fossil fuel, which is believed to be limited, while a significant amount of alternative energy is available, such as biofuel, hydroelectric power, and wind energy. In addition, hydrogen (H_2) and fuel cells are perceived as some of the most clean and efficient energy resources and devices.

Some fuel cells must use highly purified H_2 as the fuel gas; proton-exchange membrane fuel cells (PEMFCs) that work at mild temperature (usually lower than 100°C) and others can use carbon-based fuels, such as methane, carbon monoxide and so on [1].

Solid oxide fuel cells (SOFCs) have good application prospects in submarine and auxiliary power units (APUs), among others. SOFCs are high-temperature fuel cells

Nomenclature

A	pre-exponential constant/$mol \cdot m^{-3} \cdot s^{-1}$		V_{pol}	polarization voltage/V
a	characterizing the cell size/m		x_i	molar fraction of gas species i
c_p	specific heat at constant pressure/$J \cdot kg^{-1} \cdot K^{-1}$		Y_i	mass fraction of species i
$D_{i,j,eff}$	effective diffusion coefficient		ε	porosity
E	activation energy/$kJ \cdot mol^{-1}$		η_{act}	activation over-potential/V
i	current density/$A \cdot m^{-2}$		κ	permeability of porous media
i_0	exchange current density/$A \cdot m^{-2}$		μ	dynamic viscosity/$N \cdot s \cdot m^{-2}$
$\vec{J_l}$	multicomponent diffusive mass flux/$kg \cdot s^{-1}$		ρ	density/$kg \cdot m^{-3}$
K_{eq}	equilibrium constant		$\sigma_{s,eff}$	effective electronic conductivity/$S \cdot m^{-1}$
k	velocity constant/$mol \cdot m^{-3} \cdot s^{-1}$		φ_s	negative gradient of electrostatic potential/V
$k_{s,eff}$	thermal conductivity/$W \cdot m^{-1} \cdot K^{-1}$		ϕ_s	potential of electrodes/V
M_i	molar mass of species i/$g \cdot mol^{-1}$		ϕ_l	potential of electrolyte/V
p	pressure of gas mixture/Pa		$\Delta\phi_{eq}$	difference of equilibrium potential/V
R_g	universal ideal gas constant/$J \cdot mol^{-1} \cdot K^{-1}$		**Subscripts, superscripts and acronyms**	
R_s	the water gas shifting reaction rate/$mol \cdot m^{-3} \cdot s^{-1}$		a	anode
T	temperature/K		c	cathode
$\vec{u}$	velocity vector/$m \cdot s^{-1}$		eff	effective
V_{cell}	cell potential/V		TPB	triple phase boundaries

(T=650–1000°C) that consist of interconnects, gas channels, anodes, cathodes, and electrolytes, and the generating efficiency has been reaching up to and above 60%. The connection is made of alloys that can transfer electrons. The electrolyte is a solid and the major ingredient is YSZ (yttria-stabilized zirconia). Anodes and cathodes consist of porous nickel/yttria-stabilized zirconia (Ni/YSZ) and lanthanum manganite (LaMnO$_3$), and the thermal properties of the porous materials are shown in Refs. [2,3]. Since SOFCs operate at high temperature, the waste heat generated by SOFCs can combine with the internal reformer that utilizes the waste heat in order to work. Circulation steam and the catalyst convert the carbon-cased fuel into hydrogen-rich fuel.

The catalyst covers the interface of the porous anode and the WGS reaction occurs at the anode [4]. Carbon monoxide does not participate in the chemical reaction and the hydrogen generated by the chemical reaction takes part in the electrochemical reaction within triple phase boundaries (TPBs) at the interface between the electrolyte and anode [5].

Steady-state performance of SOFCs has been studied in many aspects over several decades. Since SOFC fuel is complex, the effects of fuel types on SOFCs have been studied by many researchers. WU Yiyang et al. researched the temperature distribution with different methane pre-reforming percentage [6]. Climenti and Hill [7] investigated the SOFC model fed with liquid fuel, such as natural gas, methyl ether, ethyl alcohol, and some other liquid. The results show that ethyl alcohol is better

than others due to lower carbon deposition and higher current density. Girona et al. [8] performed experiments with biogas and humidified H$_2$ while establishing the model that shows a SOFC operating at high current density (i=200 A/cm^2) or with a decreasing methane concentration will reduce the formation of carbon deposits. In addition, the types of internal reforming have been studied by some researchers. Choudhary and Sanjay [9] established a three-dimensional (3-D) model to research the performance of SOFCs with direct internal reforming, investigating the carbon deposition and the influence of oxygen concentration on temperature distributions. Corigliano and Fragiacomo [10] presented a general numerical model in MatLab (MathWorks, USA) to analyze the fuel utilization (FU), oxidant utilization, and pressure. Tubular cells and planar cells are the two of the most common structures of SOFCs. Evans et al. [11,14] established a numerical model to simulate a tubular SOFC with a single cell consisting of channels, anodes, cathodes, and electrolytes. The results show that increasing the inlet temperature will reduce the current density, power density, and fuel effects. Kim et al. [5,12,13] investigated a planar-anode-supported SOFC by the numerical method. These models are used to analyze temperature distributions, thermal stress, velocity field, etc. Planar-anode-supported SOFCs are being widely used due to their excellent electrochemical performance.

However, chemical reactions and electrochemical reactions in an anode and the TPBs are complex, which

consist of many elementary reactions [15]. Therefore, it is very difficult to build a precise numerical model to describe the electrochemical performance of SOFCs.

The purpose of this study is to establish a precise 3-D thermal-fluid numerical model including electrochemical and water-gas-shift (WGS) reactions. In our study, the WGS reaction as the internal reforming reaction is considered, which depends on the mass fraction of carbon monoxide (CO), hydrogen (H_2), carbon dioxide (CO_2), and water steam (H_2O). In addition, natural convection is considered in this model, and we assume that the upper and lower surfaces of the interconnects are in contact with air. In addition, these two models, with and without considering the natural convection at the SOFC's surface, are discussed in this work, because SOFCs operate at high temperature, even though a low convection heat-transfer coefficient can influence the temperature distributions obviously.

The temperature distributions (T) and temperature gradient ($\Delta T/\Delta x$) along the gas-flow direction have been studied. These data are important for a realistic SOFC because the thermocouples can be reduced when they are used to measure the temperature of an SOFC. Thermal stress is the major cause of SOFC failure, which is caused by temperature differences within the SOFC. This is the reason that we established a 3-D modeling this work, which will allow clearer observation of the temperature profiles and gas concentration than can be achieved with one-dimensional or two-dimensional models.

2. Modeling

A 3-D thermal-fluid numerical model including electrochemical and internal WGS reactions for a single channel of a SOFC was developed. This model consists of charge-, mass-, species-momentum-, and energy-transport-conservation equations.

2.1 Geometry

As shown in Fig. 1, a single cell is composed of the connection, anode channel, anode support layer, electrolyte, cathode, and cathode channel. Because an electrochemical reaction occurs at the interface of the electrolyte and electrode, we set up an anode active layer and cathode active layer between the electrolyte and the electrode. The geometry parameters of the SOFC model are shown in Table 1.

Table 1   Dimension of the modeled SOFC

Dimension	Values/m
Cell length (l)	0.05
Anode/cathode gas channel width (w_{ch})	1×10^{-3}
Anode/cathode gas channel height (h_{ch})	1×10^{-3}
Connection width (w_c)	1×10^{-3}
Connection height (h_c)	4×10^{-4}
Anode support layer thickness (d_s)	4×10^{-4}
Anode active layer thickness (d_a)	2×10^{-5}
Electrolyte thickness (d_e)	8×10^{-6}
Cathode active layer thickness (d_{ca})	1.3×10^{-5}
Cathode thickness (d_c)	2.5×10^{-5}

2.2 Assumptions

To simplify the model and make it easy to calculate, it is necessary to make some assumptions:

(a) The temperature, velocity, and mass fraction of the inlet are known.

(b) The velocity and species concentration of the outlet boundary are fully developed.

(c) The left- and right-hand borders are symmetrical.

(d) The convective heat transfer occurs on the upper and lower surfaces, and the remaining surfaces are adiabatic.
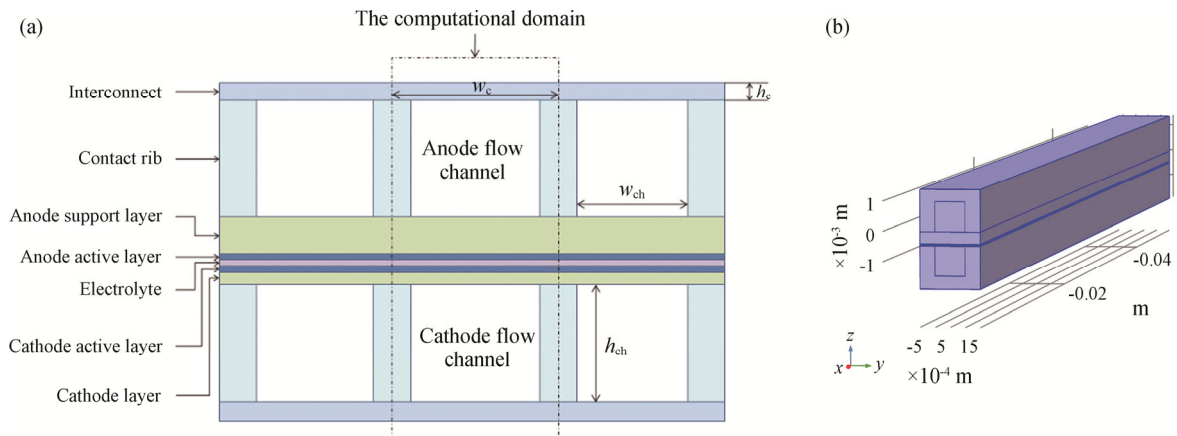

Fig. 1   (a) Schematic of SOFC and (b) geometric model of a single cell

(e) The flow within the fuel cell channel is laminar flow.

(f) The electro-chemical reactions take place at the active layer and the chemical reaction occurs at the porous anode.

(g) The boundary-layer flow is ignored.

(h) Both H_2 and CO take part in the electrochemical reaction.

(i) All of the materials are isotropic.
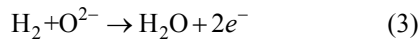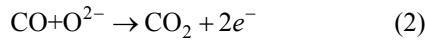
2.3 Modeling of electrochemical and chemical reactions

The inlet gas includes steam (H_2O) and CO, and these two gases will react each other:

$$CO+H_2O \rightarrow CO_2+H_2 \quad \Delta H_{1073K} = -35\,\text{kJ/mol} \quad (1)$$
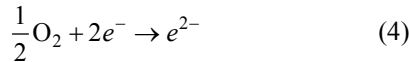
The water-gas-shift reaction (1) remains in equilibrium quickly due to high temperature and the reaction is exothermic.

An electrochemical reaction occurs at the interface of the electrolyte and electrode,

Anode:

$$CO+O^{2-} \rightarrow CO_2 + 2e^- \quad (2)$$

$$H_2+O^{2-} \rightarrow H_2O + 2e^- \quad (3)$$

Cathode:

$$\frac{1}{2}O_2 + 2e^- \rightarrow e^{2-} \quad (4)$$

Electrochemical reactions (2)–(4) are also exothermic reactions.

2.4 Governing equation

2.4.1 Continuity equation

The flow within a SOFC is modeled as follows:

$$\nabla \cdot (\varepsilon \rho \vec{u}) = S_m \quad (5)$$

where ε is the porosity of porous electrodes; ρ means the average density of the mixture; $\vec{u}$ the velocity vector of the gas mixture, and S_m is the source of production. In addition, the value of ρ is calculated by the ideal-gas law:

$$\rho = p\left(RT\sum_i \frac{Y_i}{M_i} \right)^{-1} \quad (6)$$

where p represents the pressure of mixture, T the temperature of the gas mixture, Y_i is the mass fraction, and M_i is the molar mass.

At the flow channel, there are no porous media and production, which means that ε is 1 and S_m is 0. However, at the porous electrodes, due to electrochemical and chemical reactions, the source S_m can be calculated as follows:

$$S_m = \sum_i R_i M_i \quad (7)$$

where R_i represents the rate of generation and consumption of species i.

2.4.2 Momentum equation

The momentum equation within porous electrodes is expressed as

$$\frac{\rho}{\varepsilon}\left((\vec{u} \cdot \vec{\nabla}) \frac{\vec{u}}{\varepsilon} \right) = \nabla \cdot \left[-pI + \frac{\mu}{\varepsilon}\left((\vec{\nabla} \cdot \vec{u}) + (\vec{\nabla} \cdot \vec{u})^T \right) \right. $$
$$\left. -\frac{2\mu}{3\varepsilon}(\vec{\nabla} \cdot \vec{u})I \right] - \left(\frac{\mu}{\kappa} + \vec{\nabla} \cdot (\rho \cdot \vec{u})\vec{u} \right) \quad (8)$$

where μ represents the dynamic viscosity and κ the permeability of the porous media.

2.4.3 Energy-conservation equation

The enthalpy of the electrochemical reaction is converted to electrical and thermal energy. The energy conservation equation is expressed as

$$\vec{\nabla} \cdot \left((\rho \cdot c_p)_{\text{eff}} \cdot \vec{u} \cdot T \right) = \vec{\nabla} \cdot \left(k_{\text{s,eff}} \cdot \vec{\nabla} T \right) + S_e \quad (9)$$

where c_p is the specific heat and $k_{\text{s,eff}}$ is the thermal conductivity of the porous media. The source S_e is expressed as:

$$S_e = \sigma_{\text{s,eff}} \cdot \vec{\nabla}\varphi_s \cdot \vec{\nabla}\varphi_s \quad (10)$$

where $\sigma_{\text{s,eff}}$ is the effective electronic conductivity of the electrodes and φ_s is the electrostatic potential.

2.4.4 Species-conservation equation

The species-conservation equation is a diffusion equation, and, at the flow channel and other areas without chemical and electrochemical reactions, the convection and diffusion are the main types of species transfer:

$$\vec{\nabla} \cdot \vec{J_l} + \rho\left(\vec{u} \cdot \vec{\nabla} \right)x_i = 0 \quad (11)$$

where x_i is the molar fraction of species i and $\vec{J_l}$ is the multi-component diffusive mass flux. Because the mass fraction of gases is known in this model, the molar fraction x_i can be calculated by:

$$x_i = \frac{Y_i}{M_i}\left(\sum_{i=1}^{N}(x_i \cdot M_i) \right) \quad (12)$$

and $\vec{J_l}$ by

$$\vec{J_l} = -\rho x_i \left(\sum_{j=1}^{N}\left(D_{i,j,\text{eff}} \cdot \vec{d_J} \right) \right) \quad (13)$$

where $D_{i,j,\text{eff}}$ is the effective diffusion coefficient and $\vec{d_J}$ can be calculated as follows:

$$\vec{d_J} = \vec{\nabla}X_j + \frac{(X_j - x_j)\vec{\nabla}p}{p} \quad (14)$$

X_j is calculated as follows:

$$X_j = x_j \left(M_j \left(\sum_{i=1}^{N}\frac{x_i}{M_i} \right) \right)^{-1} \quad (15)$$

However, at the porous electrodes, chemical and electrochemical reactions influence the species

conservation.

Chemical reaction (1) occurs at anode support layer and it achieves equilibrium quickly and remains in equilibrium immediately. We use the Arrhenius equation to describe the water-gas-shift reaction rate, which is expressed as:

$$R_s = k \cdot \left(p_{CO} p_{H_2O} - \frac{p_{CO_2} p_{H_2}}{K_{eq}} \right) \tag{16}$$

where K_{eq} is the equilibrium constant and p_{CO}, p_{H_2O}, p_{CO_2}, and p_{H_2} are the partial pressures of the respective species; k is the velocity constant of the WGS reaction rate, which is calculated by the following equation:

$$k = A \left(\frac{T}{T_{ref}} \right)^n \exp \left(\frac{-E}{R_g T} \right) \tag{17}$$

where A is a pre-exponential constant; E is the activation energy; R_g is the universal ideal-gas constant (J/(mol·K)), and T_{ref} is 1 K, which is shown in Table 2 [16].

Table 2　Reforming rate expression constants

Parameter	Value	Ref.
A	1.955×10^6 mol·m^{-3}·Pa^{-2}·s^{-1}	[16]
E	67130 kJ/mol	[16]
n	0	[16]

The molar rates are expressed as:

$$R_{CO} = -R_s \tag{18}$$

$$R_{H_2O} = -R_s \tag{19}$$

$$R_{H_2} = R_s \tag{20}$$

$$R_{CO_2} = R_s \tag{21}$$

as a result, the mass rates of CO, H_2O, H_2 and CO_2 are shown:

$$S_{CO} = M_{CO} \cdot R_{CO} \tag{22}$$

$$S_{H_2O} = M_{H_2O} \cdot R_{H_2O} \tag{23}$$

$$S_{H_2} = M_{H_2} \cdot R_{H_2} \tag{24}$$

$$S_{CO_2} = M_{CO_2} \cdot R_{CO_2} \tag{25}$$

where M_i represents the molar mass of mixture. The values of related parameters of porous electrodes are shown in Table 3.

2.4.5 Governing equation of electrochemical reaction

When the electrochemical reaction occurs, electric charges are transferred and generate current, which is expressed by the Butler volume equation:

Table 3　Physical properties of porous electrodes

Physical property	Symbol	Value	Ref.
Effective electronic conductivity of anode	$\sigma_{sa,eff}$	4800 S/m	[5]
Effective electronic conductivity of cathode	$\sigma_{sc,eff}$	1600 S/m	[5]
Effective thermal conductivity of anode	$k_{sa,eff}$	3 W·m^{-1}·K^{-1}	[5]
Effective thermal conductivity of cathode	$k_{sc,eff}$	2 W·m^{-1}·K^{-1}	[5]
Anode material specific heat	$c_{p,a}$	595 J·kg^{-1}·K^{-1}	[5]
Cathode material specific heat	$c_{p,c}$	573 J·kg^{-1}·K^{-1}	[5]
Anode material specific density	ρ_a	6870 kg·m^{-3}	[5]
Cathode material specific density	ρ_c	6570 kg·m^{-3}	[5]

$$i = i_0 \left[\exp \left(\frac{\alpha_a F}{RT} \eta_{act} \right) - \exp \left(-\frac{\alpha_c F}{RT} \eta_{act} \right) \right] \tag{26}$$

where R is ideal gas constant. T is operating temperature, α is the coefficient of activation energy and F is Faraday constant. The electrochemical processes at the anode include two parts: H_2-H_2O and CO-CO_2 oxidation, which can be expressed by:

$$i_{0,a}^{H_2} = i_{H_2} \left[\frac{\left(\frac{p_{H_2}}{p_{ref}} \right)^{\frac{1}{4}} \cdot \left(p_{H_2O} \right)^{\frac{3}{4}}}{1 + \left(\frac{p_{H_2}}{p_{ref}} \right)^{\frac{1}{2}}} \right] \tag{27}$$

$$i_{0,a}^{CO} = i_{CO} \left[\frac{\left(\frac{p_{CO}}{p_{ref}} \right)^{\frac{1}{4}} \cdot \left(p_{CO_2} \right)^{\frac{3}{4}}}{1 + \left(\frac{p_{CO}}{p_{ref}} \right)^{\frac{1}{2}}} \right] \tag{28}$$

At the cathode, the electrochemical process mainly includes O_2 reduction, which is expressed in a similar way:

$$i_{0,c} = i_{0,c}^{O_2} = i_{O_2} \left[\frac{\left(\frac{p_{O_2}}{p_{ref}} \right)^{\frac{1}{4}}}{1 + \left(\frac{p_{O_2}}{p_{ref}} \right)^{\frac{1}{2}}} \right] \tag{29}$$

where i is the current density and i_0 the exchange current density, which means that the electrode reaction is in dynamic balance; that is, the rate of the forward reaction is the same to the rate of the reverse reaction. η_{act} is the activation over-potential, which is defined as:

$$\eta_{act} = \phi_s - \phi_l - \Delta\phi_{eq} \tag{30}$$

where $\Delta\phi_{eq}$ is the difference in the equilibrium potential, ϕ_s and ϕ_l are the potentials of the electrodes and

electrolyte, respectively. At the anode boundary, the potential is zero-potential reference and at the cathode boundary the potential is the cell potential V_{cell}:

$$V_{cell} = \Delta\phi_{eq,c} - \Delta\phi_{eq,a} - V_{pol} \qquad (31)$$

where V_{pol} is the polarization voltage. In this model, $\Delta\phi_{eq,a}$=0 V and $\Delta\phi_{eq,c}$=1 V.

The parameters of the electrochemical reaction are shown in Table 4.

2.5 Boundary conditions

In this study, there are some boundary conditions:

At the inlet of the gas-flow channel, the velocity, temperature, and species concentrations of the gases are known:

$$u_{in}=u_0, \; Y_{in}=Y_0, \; T_{in}=T_0$$

The flow channel is long enough and the fluid has developed fully at the outlet.

A fuel-cell unit is analyzed and the convective heat transfer occurs on the upper and lower surfaces, and the remaining surfaces are adiabatic.

Table 4 Properties of active layers

Physical property	Symbol	Value	Ref.
Active surface area	A_S	$1.025\times10^5 \, m^{-1}$	[5]
Anodic exchange current density, H_2-H_2O	i_{0,H_2}	5300 A/m^2	[17]
Anodic exchange current density, CO-CO_2	$i_{0,CO}$	1700 A/m^2	[18]
Cathodic exchange current density	$i_{0,c}$	2300 A/m^2	[17,18]
Anodic charge-transfer coefficient, anode	α_a^a	2	[17]
Cathodic charge-transfer coefficient, anode	α_c^a	1	[5]
Anodic charge-transfer coefficient, cathode	α_a^c	1.5	[5]
Cathodic charge-transfer coefficient, cathode	α_c^c	0.5	[5]
Effective anode ionic conductivity	$\sigma_{ea,eff}$	0.29 S/m	[5]
Effective cathode ionic conductivity	$\sigma_{ec,eff}$	0.24 S/m	[5]

The interface of the fluid and solid meets no slip condition, and the left- and right-hand borders meet a symmetry condition.

2.6 Model verification

The computational domain is meshed with 79 200 finite-volume elements. When the number of elements is increased or decreased by half along an arbitrary direction, the results of simulation are not obvious. As the result, we use the meshing given in Table 5 to perform the simulation.

Very few researchers have studied the issue of fuel-cell gas including CO and H_2, especially experimentally. Therefore, it is difficult to verify this model with experimental data. However, there are many researchers who have researched SOFCs fed with H_2 only. The electrochemical sub-model was verified using experimental data [20] taken at 600°C.

To make the validation more accurate, we set the same operating conditions and same model parameters in this model. As shown in Fig. 2(a), the errors of experimental data and simulation are within acceptable limits. Therefore, we can consider that the electrochemical model is accurate under these operating conditions.

Table 5 Meshing of computational domain

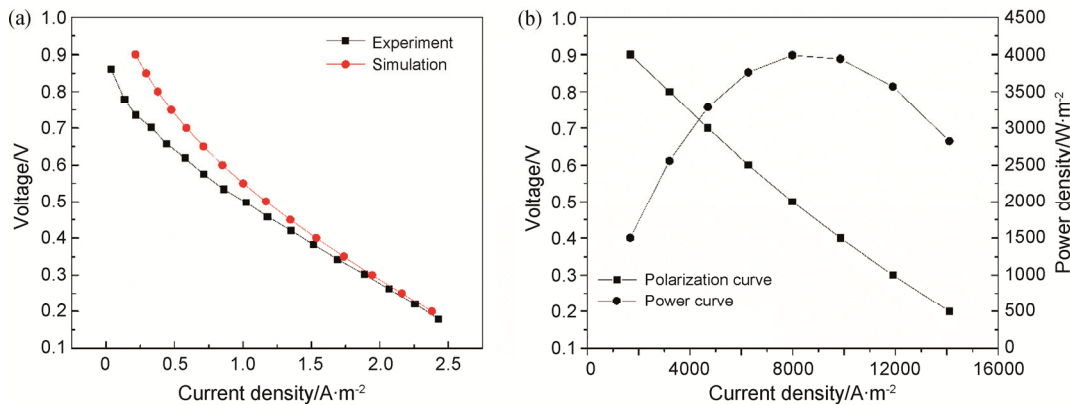| Dimension	Number of elements
Cell length (l)	60
Anode/cathode gas channel width (w_{ch})	10
Anode/cathode gas channel height (h_{ch})	10
Connection width (w_c)	5
Connection height (h_c)	10
Anode support layer thickness (d_s)	8
Anode active layer thickness (d_a)	8
Electrolyte thickness (d_e)	5
Cathode active layer thickness (d_{ca})	8
Cathode thickness (d_c)	8

Fig. 2 (a) Polarization curve of experimental data and simulation result and (b) polarization and power density curves

3. Results and Discussion

3.1 Polarization and power-density curves

Fig. 2(b) shows the basic electrical parameter, indicating that the cell voltage and power change with current density by power-density curves and the polarization. When a SOFC is used as a generator, the output power as the important parameter is worthy of study. A SOFC can reach a maximum power density P_{mp}=4246 W/m^2 if the operating voltage V_{cell} is approximately 0.5 V and the current density to J=8441 A/m^2. When the current density is less than 8441 A/m^2, the output power decreases with decreasing current density, and when the current density is greater than 8441 A/m^2, the output power decreases with increasing current density.

3.2 Temperature field

Since SOFCs are high-temperature fuel cells, the operating temperature is 1073 K, and the anode gas temperature and cathode gas temperature are also 1073 K. The heat convection between the fuel cell and air is small and the heat-transfer coefficient is 5 W/(m^2·K).

Fig. 3(a) shows the temperature profiles along the interface between the anode support layer and the anode active layer at different operating voltages. As can be seen from the curve, the temperature decreases gradually along the x axis when the voltage is higher than 0.5 V and increases gradually along the x axis when the voltage is lower than 0.6 V.

In Fig. 3(b), the temperature of the SOFCs increases along the x axis at different operating voltages without considering the heat convection between both surface and environment.

Heat generated from fuel cells mainly comes from chemical and electrochemical reactions. Since chemical reaction (1) and electrode reactions (2) and (3) are exothermic reactions, the reaction rate is faster and the temperature of the FCs is higher.

In contrast with Fig. 3(b), Fig. 3(a) shows a downward trend at high voltage. The heat convection between SOFCs and air is important to the study of temperature distributions. It can be observed that the heat convection is the major factor in dissipating the internal heat generated.

Fig. 4 shows an isograph of the longitudinal cross-section of a SOFC. From the isograph, it can be seen that the heat is mainly concentrated in the center of anode and electrolyte, where the WGS reaction and electrochemical reactions exist. In the anode support layer, temperature distributions are disproportionate, which will induce thermal stresses. The thermal stresses

between the different materials in SOFCs will cause extrusion of electrode and electrolyte, which will leads to leakage and damage.
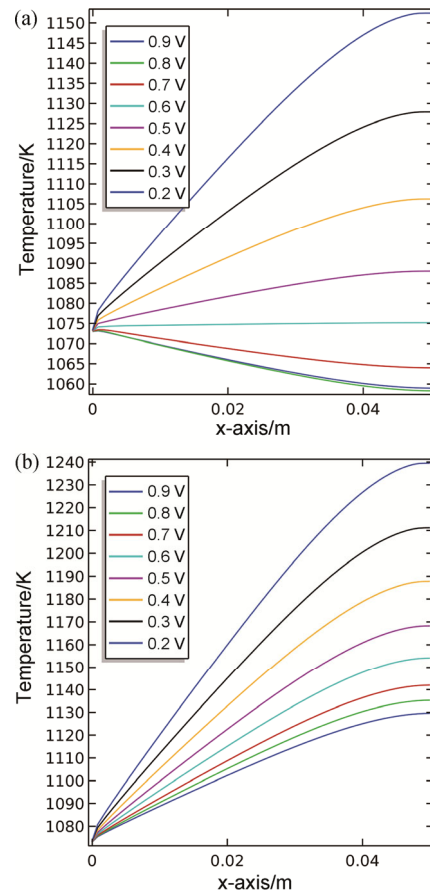

Fig. 3 (a) Considering and (b) without considering the heat-convection temperature profiles along the x axis at interface between the anode support and active layers at different voltages
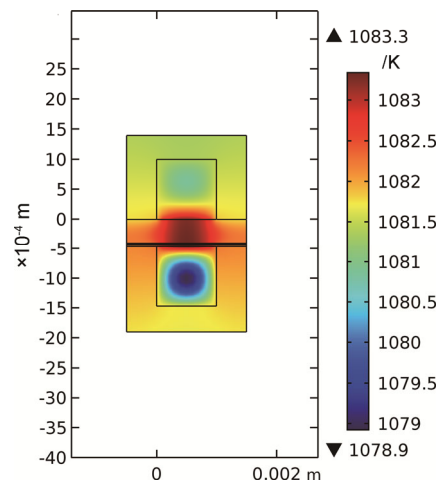

Fig. 4 Isograph of longitudinal cross-section of SOFC at an operating voltage of 0.5 V

Fig. 5 shows the temperature gradient ($\Delta T/\Delta x$) along the *x* axis at the interface between the anode support and active layers. At the inlet of SOFCs, the temperature gradient decreases rapidly and gradually at the latter section of SOFCs.

Fig. 5(a) shows the small temperature difference and that the temperature gradient is lower than 1000 K/m along the *x* axis, which means that the thermal stress of the SOFC is small. The temperature gradient decreases by 30% due to the heat convection. In this model, the natural convection is set as the least value, i.e. 5 W/(m²·K).

In addition, the different operating voltages influence the temperature gradient seriously. The average minimum temperature gradient does not appear at the maximum voltage or the minimum voltage. When the operating voltage is under middle voltage, the temperature gradient is the minimum. The average temperature gradient at the middle voltage is little higher than the temperature at the middle voltage. While at the low operating voltage, the average temperature gradient is higher than the temperature at the middle and high voltage.

Next, how the case A: co-flow and case B: counter-flow influence the temperature will be analyzed in our study. According to the previous literature, the counter flow will cause the more current density, while the effect of flow type on temperature gradient will be studied.

Fig. 6(a) and (b) shows the temperature gradient distribution along x-axis with case A and case B. At the middle operating voltage, the temperature gradient is at the low value with case A or case B. Therefore, operating at the middle voltage will increase the life of the SOFC. Besides, at the low voltage, due to electrochemical reactions violent, the temperature gradient will be more than the temperature gradient at high voltage.

In addition, when the direction of fuel flow and air flow is different, the temperature direction will be complex. From the Fig. 6(a) and the Fig. 6(b), the average temperature gradient of counter flow higher than the temperature gradient of co-flow, and the maximum temperature gradient of counter flow occurs both the
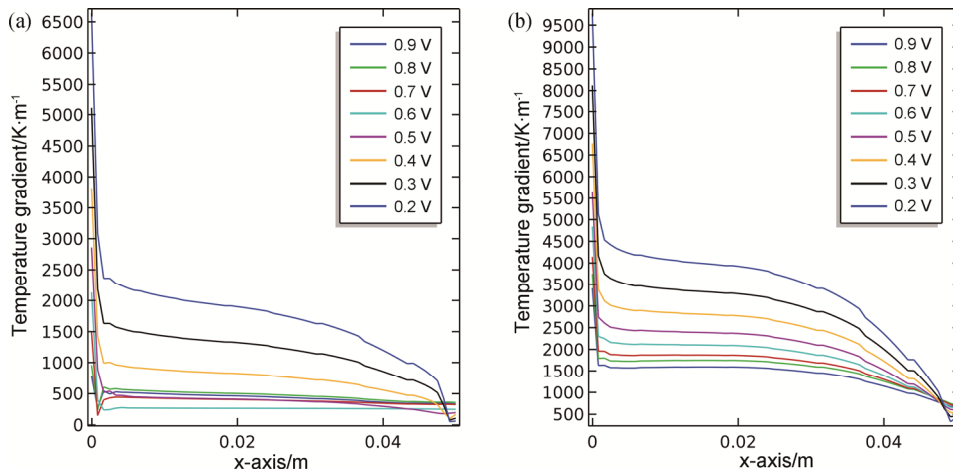

Fig. 5   (a) Considering and (b) without considering the heat-convection temperature gradient ($\Delta T/\Delta x$) along the *x* axis at the interface between the anode support and active layers. V_{cell} is varied from 0.2 to 0.9 V.
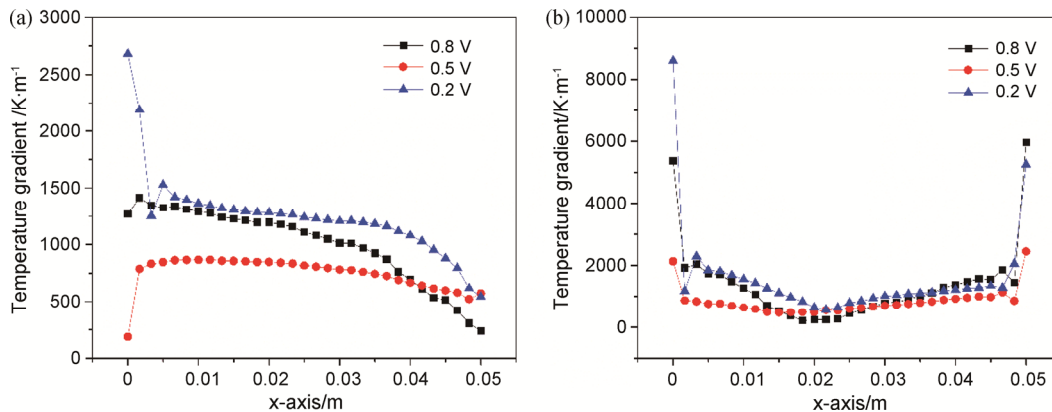

Fig. 6   (a) Co-flow and (b) counter flow temperature gradient ($\Delta T/\Delta x$) along the *x* axis at the interface between the anode support and active layers

ends of the channels, which needs more attention in practice experiment.

3.3 Component concentration

The mass fraction, gas species and velocity of the anode and cathode inlet are given. The anode inlet mass fractions of mixture are $Y_{in,i,a}$=0.05, 0.6, 0.3, and 0.05, respectively, for i=H_2, CO, H_2O, and CO_2. CO can react with H_2O. According to relevant research, when the steam-to-carbon (S/C) ratio is higher than 2 in SOFCs, there are no C deposits covering the electrode surface. At

the cathode inlet, we use air as the oxidizing agent, and the inlet mass fractions of air are $Y_{in,i,c}$=0.23, 0.76, and 0.01, respectively, for i=O_2, N_2, and H_2O. The anode inlet velocity is 5 m/s and the cathode inlet velocity is 11 m/s.

Fig. 7(a)–7(d) show the molar-fraction cloud diagram of fuel-gas concentration distributions at 0.5 V.

It is clear that CO and H_2 molar concentration decreases gradually from inlet to outlet. CO reacts with vapor, producing H_2 and CO_2, which decreases the concentration of CO and increases that of CO_2.

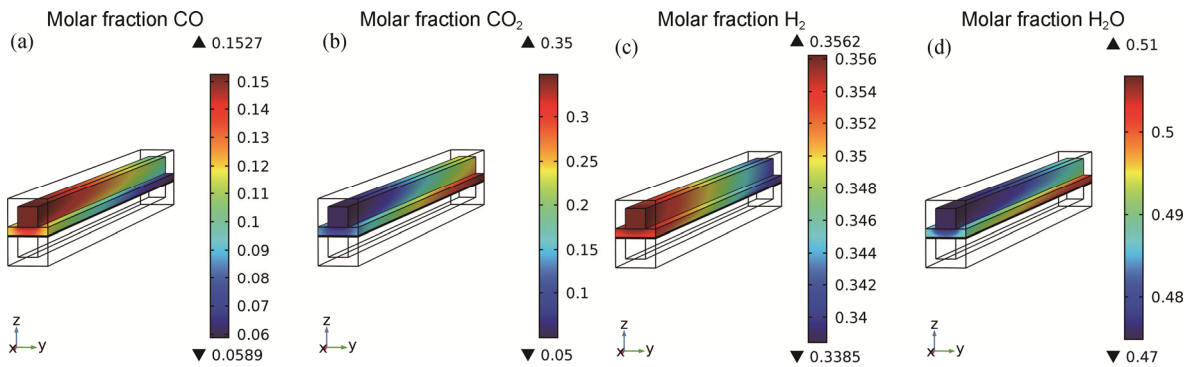Fig. 8 shows CO and H_2 molar fractions along the x

Fig. 7   Molar-fraction cloud diagrams of (a) CO, (b) CO_2, (c) H_2, and(d) H_2O.
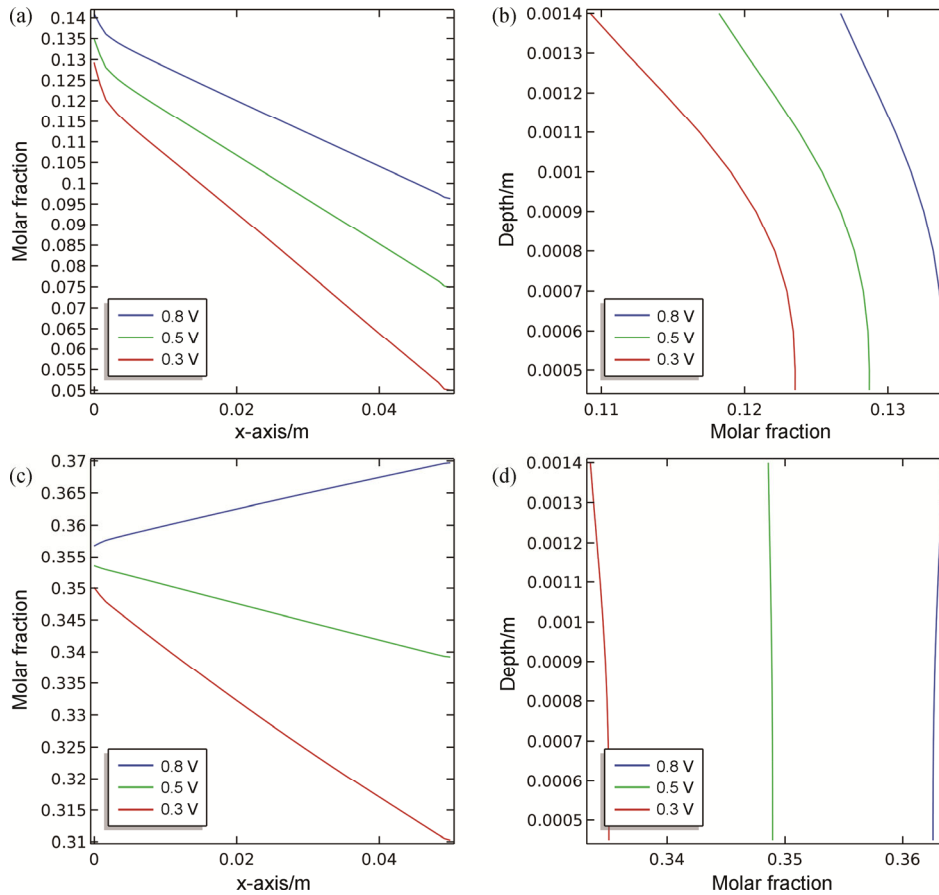

Fig. 8   (a) (b) CO and (c)(d) H_2 molar fractions along the x axis at the interface between the anode support and active layers and along the depth (z axis) at the center (x=0.025 m) of the channel at 0.3, 0.5, and 0.8 V.

axis and the depth at the center of the channel at different operating voltages. As the voltage decreases, the consumption of H_2 and CO increases due to increasing chemical and electrochemical reaction rates.

At a voltage of 0.8 V, the H_2 molar fraction increases along the x axis because the generation of H_2 is greater than its consumption, which will cause low fuel utilization.

3.4 Fuelutilization

The FU is calculated by:

$$U_f = 1 - \frac{\dot{n}_{H_2,out} + \dot{n}_{CO,out}}{\dot{n}_{H_2,in} + \dot{n}_{CO,in}} \qquad (32)$$

where $\dot{n}_{H_2,in/out}$ and $\dot{n}_{CO,in/out}$ is the inlet and outlet molar flux (in mol·s^{-1}) of H_2 and CO, respectively.

Fig. 9 shows that the FU along the x axis at different operating voltages. It is clear from the curve that the fuel utilization increases gradually along the x axis. Since H_2 can be generated through a chemical reaction, not much CO is consumed and FU is low. Through the analysis of component concentration, at low voltage, the chemical and electrochemical reactions are faster and therefore the FU is higher at low voltage.
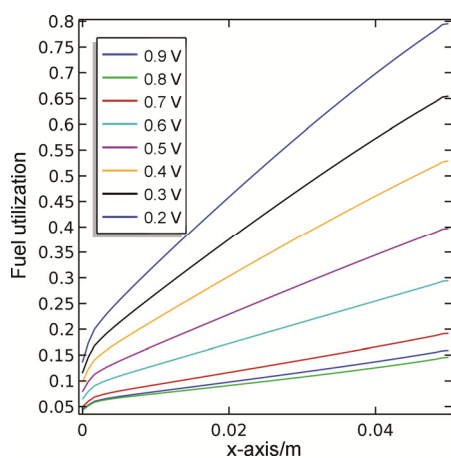

Fig. 9 FU along the x axis at different operating voltages

4. Conclusions

A 3-D thermal-fluid numerical model including an electrochemical reactions and direct internal reforming reaction for a single channel SOFC was established. The polarization curve, power curve, temperature, temperature gradient, molar-fraction distributions of fuel gases, and FU were studied at different operating voltages.

In this work, we considered the effect of natural convection on temperature distributions, which occurred at upper and lower surfaces, and the convection

heat-transfer coefficient was assumed to be 5 W/(m^2·K). It was clear that the natural convection had a great impact on the SOFCs. Even at high voltage, the heat generated by chemical and electrochemical reactions was not enough to offset the heat consumed by natural convection, which caused temperature to decrease along the fuel-cell length. The distributions of the temperature gradient ($\Delta T/\Delta x$) largely represented the thermal stress, which was the most important parameter for SOFCs. The temperature gradient was a maximum at the inlet and decreased along the cell length.

The molar fraction of the hydrogen and carbon monoxide has been studied. Interestingly, the hydrogen molar fraction increased at the high voltage while decreased at the middle and low voltage, because the low temperature caused by the high voltage will result in decrease of rate of chemical reaction and forward electrochemical reaction, which caused that the produce of hydrogen was higher than the consume of the hydrogen. Through analyzing the depth of the anode and flow channel gas molar fraction, i.e. the direction of the z, we can know that in the flow channel, the diffusion of gas was faster than it in the porous anode due to the flow resistance, which will influence the performance of the fuel cell.

The simulation data gathered in this study are valuable in predicting the temperature distributions, which will reduce the number of thermocouples on SOFCs. Carbon deposition took place in SOFCs fed with C-based fuel, the degree of which can be predicted by the component concentration distributions. However, it is necessary to study the dynamic model to develop the necessary control strategy. In the future studies, the dynamic simulation will be studied.

Acknowledgements

References

[1] Janardhanan V.M., Deutschmann O., Modeling of solid-oxide fuel cells. Zeitschrift Für Physikalische Chemie (English: Journal of Physical Chemistry), 2007, 221(4): 443–478.

[2] Madejski P., Krakowska P., Habrat M., Puskarczyk E., Jędrychowski M., Comprehensive approach for porous materials analysis using a dedicated preprocessingtool for mass and heat transfer modeling. Journal of Thermal Science, 2018, 27(05): 479–486.

[3] Guo C.S., Nian X.B, Liu Y., Qi C., Song J.S., Yu W.H., Analysis of 2D flow and heat transfer modeling in

fracture of porous media. Journal of Thermal Science, 2017, 26(04): 331–338.

[4] Spiegel C., Designing and building fuel cells. McGraw-Hill, 2007.

[5] Nerat M., Juričić Đ., A comprehensive 3-D modeling of a single planar solid oxide fuel cell. International Journal of Hydrogen Energy, 2016, 41(5): 3613–3627.

[6] Wu Y.Y., Shi Y.X., Cai N.S., Ni M., Thermal modeling and management of solid oxide fuel cells operating with internally reformed methane. Journal of Thermal Science, 2018, 27(03): 203–212.

[7] Cimenti M., Hill J.M., Direct utilization of liquid fuels in SOFC for portable applications: Challenges for the selection of alternative anodes. Energies, 2009, 2(2): 377–410.

[8] Girona K., Laurencin J., Fouletier J., et al., Carbon deposition in CH_4/CO_2, operated SOFC: Simulation and experimentation studies. Journal of Power Sources, 2012, 210(4): 381–391.

[9] Choudhary T., Sanjay. Computational analysis of IR-SOFC: Transient, thermal stress, carbon deposition and flow dependency. International Journal of Hydrogen Energy, 2016, 41(24): 10212–10227.

[10] Corigliano O., Fragiacomo P., Numerical simulations for testing performances of an indirect internal CO_2 reforming solid oxide fuel cell system fed by biogas. Fuel, 2017, 196: 378–390.

[11] Evans W.K., Rattanakornkan K., Suksangpanomrung A., et al., The simulations of tubular solid oxide fuel cells (SOFCs). Chemical Engineering Journal, 2011, 168(3): 1301–1310.

[12] Kim Y.J., Min C.L., Numerical investigation of flow/heat transfer and structural stress in a planar solid oxide fuel cell. International Journal of Hydrogen Energy, 2017, 42(29): 18504–18513.

[13] Dehimi S., Haddad D., Mebarki B., et al., Thermal field under the effect of the chemical reaction of a direct internal reforming solid oxide fuel cell DIR-SOFC. International Journal of Hydrogen Energy, 2014, 39(27): 15261–15265.

[14] Lackey J., Champagne P., Peppley B., Use of waste water treatment plant biogas for the operation of Solid Oxide Fuel Cells (SOFCs). Journal of Environmental Management, 2016, 203(2): 753–759.

[15] Hecht E.S., Gupta G.K., Zhu H., et al., Methane reforming kinetics within a Ni–YSZ SOFC anode support. Applied Catalysis A General, 2005, 295(1): 40–51.

[16] Pramuanjaroenkij A., Zhou X.Y., Kakaç S., Numerical analysis of indirect internal reforming with self-sustained electrochemical promotion catalysts. International Journal of Hydrogen Energy, 2010, 35(13): 6482–6489.

[17] Cui D., Liu L., Dong Y., et al., Comparison of different current collecting modes of anode supported micro-tubular SOFC through mathematical modeling. Journal of Power Sources, 2007, 174(1): 246–254.

[18] Xie Y., Ding H., Xue X., Direct methane fueled solid oxide fuel cell model with detailed reforming reactions. Chemical Engineering Journal, 2013, 228(14): 917–924.

[19] Ahmed K., Föger K., Analysis of equilibrium and kinetic models of internal reforming on solid oxide fuel cell anodes: Effect on voltage, current and temperature distribution. Journal of Power Sources, 2017, 343: 83–93.

[20] Leng Y.J., Chan S.H., Jiang S.P., et al., Low-temperature SOFC with thin film GDC electrolyte prepared in situ by solid-state reaction. Solid State Ionics, 2004, 170(1): 9–15.